Improved Interface conditions for 2D domain decomposition with corners: Numerical applications

Chokri Chniti, Frédéric Nataf, Francis Nier

Improved Interface conditions for 2D domain decomposition with corners: Numerical applications

Chokri Chniti
CMAP, UMR CNRS 7641
Ecole Polytechnique
F- 91128 Palaiseau Cedex

Frédéric Nataf
Laboratoire Jacques-Louis Lions,
UMR CNRS 7598
F-75252 Paris, Cedex 05

Francis Nier
IRMAR, UMR CNRS 6625
Université de Rennes I, Campus de Beaulieu
F-35042 Rennes Cedex

June 12, 2006

Abstract: This article deals with a local improvement of domain decomposition methods for 2-dimensional elliptic problems for which either the geometry or the domain decomposition presents conical singularities. After explaining the main results of the theoretical analysis carried out in [4], the numerical experiments presented in this article confirm the optimality properties of the new interface conditions.

Contents

1 Introduction

Domain decomposition algorithms are often introduced artificially in order to facilitate or make possible large computations. Sometimes they occur in the original model with a natural piecewise presentation. These methods are now well understood in the case of a regular domain decomposed into regular subdomains, see for example [2],[20] and [23]. A significant challenge for the applications is a good understanding of the singular cases, for example problems with corners in 2D. The general principle of those methods is as follows:

1. For an elliptic differential operator L, a domain Ω and a given right-hand side f,

consider the problem of finding u such that

$$\left\{ \begin{array}{ll} Lu & = f \text{ in } \Omega \\ & +B.C. \text{ on } \partial\Omega\,. \end{array} \right. \tag{1}$$

2. When the domain Ω is large from the numerical complexity point of view or complex from the modeling or geometrical point of view, it can be decomposed into subdomains, $\overline{\Omega} = \cup_{i=1}^{i=N} \overline{\Omega_i}$ where each Ω_i is an open subdomain of Ω.

3. The initial problem (1) is then approximated by an iterative process: the step $n+1$ is determined by solving

$$\left\{ \begin{array}{rll} Lu_i^{n+1} & = f & \text{in} \quad \Omega_i \\ B_{ij}\gamma_{ij}u_i^{n+1} & = B_{ij}\gamma_{ij}u_j^n & \text{on} \quad \partial\Omega_i \cap \overline{\Omega_j}(i \neq j) \\ & +B.C. & \text{on } \partial\Omega_i \cap \partial\Omega \end{array} \right. \tag{2}$$

simultaneously in all subdomains Ω_i, $i = 1, ..., N$.

The interface operators B_{ij} can be differential or pseudodifferential operators applied to the traces vectors $\gamma_{ij}u$. The choice of the interface operators has a great influence on the speed of convergence of the algorithm. Cases are known where for a given geometry the change of B_{ij} transforms the absence of convergence into the exact convergence after a finite number of iterations. Within the framework of the regular interfaces, this analysis has already been done theoretically and numerically. A good final choice actually relies on a compromise between the theoretical optimality and the ease of implementation, see [12][20].
In the situation with geometrical singularities one can consider two situations:

1. The global domain Ω is regular and thus the global solution is a priori more regular than the solution of the problem in every subdomain with only a piecewise-C^1 boundary.

2. The global domain is polygonal and possibly non-convex. Thus the global solution present singularities which may not appear in the solutions of the (possibly regular) subdomain problems with selected interface conditions.

We study in this paper the influence of the transmission conditions on the Schwarz algorithm for the operator $\eta - \Delta$ with $\eta > 0$. Improved transmission conditions with second order tangential derivative which were derived from an asymptotic analysis around the corner in [4] of the Schwarz algorithm, are now numerically tested. The theoretical optimality of the

asymptotic analysis relying on the matching of the main singularities within Kondratiev's theory is supported by the numerical computations.

The article is organized as follows: After the presentation of the domain decomposition method with the selected interface conditions at the corner (Section 2), we write its variational formulation both at the continuous and discrete level in Section 3. In Subsection 3.4, the refined mesh around the corner is introduced in order to catch accurately the corner singularities. In Section 4, several numerical tests carried out with the FreeFem++ software support the theoretical approach of [4]. In all cases, the minimal number of iterations is achieved when the interface transmission conditions are chosen according to [4] and additional tests are done in order to eliminate any irrelevant numerical artefact.

2 The interface conditions

We shall use polar coordinates $(r, \theta) \in \mathbb{R}_+^* \times [\theta_0, \theta_+]$ in order to develop the analysis of this domain decomposition around the corner, $r = 0$, . We work in the sectorial domain $\Omega = \mathbb{R}_+^* \times (\theta_0, \theta_+) \subset \mathbb{R}^2$, or $\Omega = \mathbb{R}^2 = (\mathbb{R}_+^* \times S^1) \cup \{O\}$ where S^1 is the unit circle. On this simple geometry, we consider the model boundary value problem (1) with $L = \eta - \Delta$, $\eta > 0$. For such a second order elliptic partial differential operators and when the interfaces are regular, the practically used and efficient interface boundary conditions involve the second order tangential derivative

$$B_{ij}(\frac{\partial u}{\partial \nu}, u) = \frac{\partial u}{\partial \nu} + \beta u - \frac{\partial}{\partial \tau}(\frac{\alpha}{2}\frac{\partial}{\partial \tau})u$$

where $\frac{\partial}{\partial \nu}$ and $\frac{\partial}{\partial \tau}$ respectively denote the normal derivative and the tangential derivative.

When $\Omega = \mathbb{R}^2 = \mathbb{R}_x \times \mathbb{R}_\tau$ is split into two half-planes, $\{x < 0\}$ and $\{x > 0\}$, and for a given bounded set of frequencies in the tangential variable with the size proportional to $1/h$ when h is the characteristic mesh size of the numerical discretization, there is an optimal choice of (α, β) for the convergence of the domain decomposition process (2). By introducing the error at step n, $e_i^n(x, \tau) = u_i^n - u$ and its Fourier transform in the tangential variable $\widehat{e}_i^n(x, k)$, the optimized coefficients $\alpha_{opt} > 0$ and $\beta_{opt} > 0$ are determined according to [12]

by the max-min problem

$$\min_{\alpha,\beta\in\mathbb{R}} \max_{|k|\leq \frac{\pi}{h}} |\rho(k;\alpha,\beta)| \tag{3}$$

$$\text{with} \qquad \varrho(k;\alpha,\beta) = \frac{\widehat{e}_i^{n+2}(0,k)}{\widehat{e}_i^{n}(0,k)} = \left(\frac{-\sqrt{\eta+k^2}+\beta+\alpha k^2/2}{\sqrt{\eta+k^2}+\beta+\alpha k^2/2} \right)^2$$

Here our domain $\Omega = \mathbb{R}_+^* \times (\theta_0, \theta_+)$ or $\Omega = \mathbb{R}^2$, is decomposed into two sectors $\Omega_1 = \mathbb{R}_+^* \times (\theta_-, \theta_+)$ and $\Omega_2 = \mathbb{R}_+^* \times (\theta_0, \theta_-)$ (with the convention $\theta_0 = \theta_+ - 2\pi$ when $\Omega = \mathbb{R}^2$). In polar coordinates, the previous boundary operator now takes the form

$$B_{ij}(\pm\frac{\partial}{r\partial\theta}u, u) = \pm\frac{\partial}{r\partial\theta}u + \beta_{opt}u - \frac{\alpha_{opt}}{2}\frac{\partial^2}{\partial r^2}u\,. \tag{4}$$

Following the approach presented in [4] (see also the discussion in [22]), the good interface boundary conditions should have the form $\pm\frac{\partial}{r\partial\theta} + \frac{\beta_\pm}{r} - \frac{\partial}{\partial r}\frac{\alpha_\pm r}{2}\frac{\partial}{\partial r}$ around the corner $r = 0$ with $\alpha_\pm$ and $\beta_\pm$ constant. Far from the corner, the interface boundary must keep the optimal form (4) of the case without corner. A synthesis of this is done by taking

$$B_{ij}(\pm\frac{\partial}{r\partial\theta}u, u) = \pm\frac{\partial}{r\partial\theta}u + \tilde{\beta}_\pm(r)u - \frac{\partial}{\partial r}\frac{\tilde{\alpha}_\pm(r)}{2}\frac{\partial}{\partial r}u \tag{5}$$

$$\text{with} \qquad \tilde{\alpha}_\pm(r) = \begin{cases} \alpha_\pm r & \text{if } r \leq \frac{\alpha_{opt}}{\alpha_\pm} \\ \alpha_{opt} & \text{if } r \geq \frac{\alpha_{opt}}{\alpha_\pm} \end{cases} \qquad \tilde{\beta}_\pm(r) = \begin{cases} \frac{\beta_\pm}{r} & \text{if } r \leq \frac{\beta_\pm}{\beta_{opt}} \\ \beta_{opt} & \text{if } r \geq \frac{\beta_\pm}{\beta_{opt}} \end{cases} \tag{6}$$

with $\alpha_\pm > 0$ and $\beta_\pm \geq 0$.

In the subdomain Ω_1, one is led to consider the boundary value problem

$$\begin{cases} \Big(\eta - \frac{1}{r^2}((r\partial_r)^2 + \partial_\theta^2)\Big)u_1^{n+1}(r,\theta) &= f \\ \Big(-\frac{1}{r}\partial_\theta - \tilde{\beta}_+(r) + \frac{1}{2}\partial_r(\tilde{\alpha}_+(r)\partial_r)\Big)u_1^{n+1}(r,\theta_+) &= \Big(-\frac{1}{r}\partial_\theta - \tilde{\beta}_+(r) + \frac{1}{2}\partial_r(\tilde{\alpha}_+(r)\partial_r)\Big)u_2^{n}(r,\theta_+) \\ \Big(-\frac{1}{r}\partial_\theta + \tilde{\beta}_-(r) - \frac{1}{2}\partial_r(\tilde{\alpha}_-(r)\partial_r)\Big)u_1^{n+1}(r,\theta_-) &= \Big(-\frac{1}{r}\partial_\theta + \tilde{\beta}_-(r) - \frac{1}{2}\partial_r(\tilde{\alpha}_-(r)\partial_r)\Big)u_2^{n}(r,\theta_-) \end{cases} \tag{7}$$

with the first boundary condition possibly replaced by the global boundary condition when $\{\theta = \theta_+\} = \partial\Omega \cap \overline{\Omega_1}$. A similar boundary value problem with possibly other pairs $(\alpha_\pm, \beta_\pm)$ or with the global boundary conditions is written for any Ω_j, $j = 2, \ldots, N$.

3 Variational formulation

After ensuring an appropriate variational formulation of the continuous subdomain problem (7) (with a straightforward adaptation to all possible combinations of boundary conditions),

the discrete variational formulation is presented with a trick which avoids the computation of discretized normal derivatives. Finally, a refined mesh process is introduced in order to get an accurate numerical results around the corner.

3.1 Continuous problem

The variational space and the variational formulation of the subdomain problem (7) are first specified in the continuous setting. Two cases are distinguished $\beta_\pm = 0$ or $\beta_\pm \neq 0$ with different variational spaces. The case $\beta_\pm \neq 0$ is not permitted when the general solution of the complete problem does not vanish at $r = 0$. Nevertheless considering $\beta_\pm \neq 0$ makes sense for example when one puts homogeneous Dirichlet boundary conditions on the complete problem with $\Omega = \mathbb{R}_+^* \times (\theta_0, \theta_+)$. This provides an additional flexibility in the choice of the pairs $(\alpha_\pm, \beta_\pm)$. [1]

Let Ω_1 be a sector of $\mathbb{R}^2$, $\Omega_1 = \mathbb{R}_+^* \times (\theta_-, \theta_+)$ and we note $\overline{\Omega_1}$ its closure in $\mathbb{R}^2$. The spaces of regular test functions are $\mathcal{C}_0^\infty(\overline{\Omega_1})$, which is the space of the restrictions to Ω_1 of $\mathcal{C}^\infty$ functions with compact support in $\mathbb{R}^2$, and $\mathcal{C}_0^\infty(\overline{\Omega_1} \setminus \{O\})$ the space of the elements of $\mathcal{C}_0^\infty(\overline{\Omega_1})$ whose support does not meet the corner O. These two spaces contain the space $\mathcal{C}_0^\infty(\Omega_1)$ of interior test functions and permit the analysis of weak formulations up to the boundary (except at the corner).

The variational spaces in order to estimate all the terms involved in the variational formulation of (7) are defined according to:

- G^1 is the completion of $\mathcal{C}_0^\infty(\overline{\Omega_1})$ for the norm $\| \ \|_{G^1}$ given by

$$\|u\|_{G^1}^2 = \int_{\Omega_1} |u|^2 (x) + |\nabla u|^2 (x) \ dx + \int_{\partial\Omega_1} |(r\partial_r)u|^2 \ \frac{dr}{r} \ .$$

  This norm makes G^1 a Hilbert space in which $\mathcal{C}_0^\infty(\overline{\Omega_1})$ is dense.

- G_0^1 is the completion of $\mathcal{C}_0^\infty(\overline{\Omega_1} \setminus \{O\})$ for the norm $\| \ \|_{G_0^1}$ given by

$$\|u\|_{G_0^1}^2 = \int_{\Omega_1} |u|^2 (x) + |\nabla u|^2 (x) \ dx + \int_{\partial\Omega_1} (|(r\partial_r)u|^2 + |u|^2) \frac{dr}{r} \ ,$$

  It makes G_0^1 a Hilbert space in which $\mathcal{C}_0^\infty(\overline{\Omega_1} \setminus \{O\})$ is dense.

[1] Practically, the case $\beta_\pm = 0$ is implemented by keeping a constant coefficient $\tilde{\beta}(r) = \beta_{opt}$ along the whole interface.

The definition of these spaces leads moreover to the following properties:

- $G_0^1 \subset G^1 \subset H^1(\Omega_1)$.
- any $u \in G^1$ (or $u \in G_0^1$) admits a trace in $H^{\frac{1}{2}}_{loc}(\partial\Omega_1 \setminus \{ O\})$.
- The inclusion $G_0^1 \subset G^1$ is strict. In fact G_0^1 does not even contain $\mathcal{C}_0^\infty(\overline{\Omega_1})$ since $\int_{\partial\Omega_1} |u(r)|^2 \frac{dr}{r} = +\infty$ for a smooth function which does not vanish in $r = 0$.

On these spaces we consider the following weak formulation according to two cases:

1) $\beta_\pm = 0$:

$$\forall v \in G^1, \quad a_{\alpha_\pm,0}(u,v) = L_{f,g_-,g_+}(v) \tag{8}$$

$$\text{with} \quad a_{\alpha_\pm,0}(u,v) = \int_{\Omega_1} \eta\, u(x)v(x) + \nabla u(x)\nabla v(x)\ dx + \int_0^{+\infty} \frac{\alpha_+}{2}(r\partial_r)u(r,\theta_+)(r\partial_r)v(r,\theta_+)\ \frac{dr}{r} + \int_0^{+\infty} \frac{\alpha_-}{2}(r\partial_r)u(r,\theta_-)(r\partial_r)v(r,\theta_-)\ \frac{dr}{r}$$

$$\text{and} \quad L_{f,g_-,g_+}(v) = \int_{\Omega_1} f(x)v(x)\ dx - \int_0^{+\infty} g_+(r)v(r,\theta_+)\ dr + \int_0^{+\infty} g_-(r)v(r,\theta_-)\ dr\,.$$

2) $\beta_\pm \neq 0$:

$$\forall v \in G_0^1, \quad a_{\alpha_\pm,\beta_\pm}(u,v) = L_{f,g_-,g_+}(v) \tag{9}$$

$$\text{with} \quad a_{\alpha_\pm,\beta_\pm}(u,v) = \int_{\Omega_1} \eta\, u(x)v(x) + \nabla u(x)\nabla v(x)\ dx + \int_0^{+\infty} \frac{\alpha_+}{2}(r\partial_r)u(r,\theta_+)(r\partial_r)v(r,\theta_+)\ \frac{dr}{r} + \int_0^{+\infty} \frac{\beta_+}{r}u(r,\theta_+)v(r,\theta_+)\ dr + \int_0^{+\infty} \frac{\alpha_-}{2}(r\partial_r)u(r,\theta_-)(r\partial_r)v(r,\theta_-)\ \frac{dr}{r} + \int_0^{+\infty} \frac{\beta_-}{r}u(r,\theta_-)v(r,\theta_-)\ dr$$

$$\text{and} \quad L_{f,g_-,g_+}(v) = \int_{\Omega_1} f(x)v(x)\ dx - \int_0^{+\infty} g_+(r)v(r,\theta_+)\ dr + \int_0^{+\infty} g_-(r)v(r,\theta_-)\ dr\,.$$

3.2 Variational formulation of the algorithm

Owing to a reformulation of the algorithm the computation of the normal derivative involved in these interface conditions is avoided. For the sake of simplicity we still consider a case with two subdomains, but this procedure can be adapted to any general decomposition with more than two subdomains.

Assume now that $\Omega = \mathbb{R}_+^* \times (\theta_0, \theta_+)$ is decomposed into two non overlapping subdomains $\Omega_1 = \mathbb{R}_+^* \times (\theta_-, \theta_+)$ and $\Omega_2 = \mathbb{R}_+^* \times (\theta_0, \theta_-)$ with the interface $\{\theta = \theta_-\}$. According to the general presentation (2), we restrict our attention to the additive Schwarz method

$$\left\{\begin{array}{rl} (\eta - \Delta) u_1^{n+1} &= f \quad \text{in} \quad \Omega_1 \\ u_1^{n+1}(r, \theta_+) &= 0 \\ \Big(-\frac{1}{r}\partial_\theta + \tilde\beta_1(r) - \partial_r(\frac{\tilde\alpha_1(r)}{2}\partial_r)\Big) u_1^{n+1}(r, \theta_-) &= \Big(-\frac{1}{r}\partial_\theta + \tilde\beta_1(r) - \partial_r(\frac{\tilde\alpha_1(r)}{2}\partial_r)\Big) u_2^{n}(r, \theta_-) \end{array}\right. \tag{10}$$

$$\left\{\begin{array}{rl} (\eta - \Delta) u_2^{n+1} &= f \quad \text{in} \quad \Omega_2 \\ u_2^{n+1}(r, \theta_0) &= 0 \\ \Big(\frac{1}{r}\partial_\theta + \tilde\beta_2(r) - \partial_r(\frac{\tilde\alpha_2(r)}{2}\partial_r)\Big) u_2^{n+1}(r, \theta_-) &= \Big(\frac{1}{r}\partial_\theta + \tilde\beta_2(r) - \partial_r(\frac{\tilde\alpha_2(r)}{2}\partial_r)\Big) u_1^{n}(r, \theta_-)\,. \end{array}\right. \tag{11}$$

Note that here no $\pm$ index appear because there is only one interface boundary at $\theta = \theta_-$. Meanwhile the indices 1 or 2 of the coefficients $\tilde\alpha$ and $\tilde\beta$ refer to the subdomain Ω_1 or Ω_2.

A direct discretization would require the computation of the normal derivatives along the interfaces $\{\theta = \theta_-\}$ in order to evaluate the right hand sides in the transmission conditions of (10)-(11). This can be avoided by introducing two new variables,

$$\begin{array}{rl} \lambda_1^n &= \Big(-\frac{1}{r}\partial_\theta + \tilde\beta_1(r) - \partial_r(\frac{\tilde\alpha_1(r)}{2}\partial_r)\Big) u_2^n(., \theta_-), \\ \lambda_2^n &= \Big(\frac{1}{r}\partial_\theta + \tilde\beta_2(r) - \partial_r(\frac{\tilde\alpha_2(r)}{2}\partial_r)\Big) u_1^n(., \theta_-). \end{array}$$

The algorithm then becomes

$$\left\{\begin{array}{rl} (\eta - \Delta) u_1^{n+1} &= f \quad \text{in} \quad \Omega_1 \\ u_1^{n+1}(r, \theta_+) &= 0 \\ \Big(-\frac{1}{r}\partial_\theta + \tilde\beta_1(r) - \partial_r(\frac{\tilde\alpha_1(r)}{2}\partial_r)\Big) u_1^{n+1}(r, \theta_-) &= \lambda_1^n(r) \\ & \\ (\eta - \Delta) u_2^{n+1} &= f \quad \text{in} \quad \Omega_2 \\ u_2^{n+1}(r, \theta_0) &= 0 \\ \Big(\frac{1}{r}\partial_\theta + \tilde\beta_2(r) - \partial_r(\frac{\tilde\alpha_2(r)}{2}\partial_r)\Big) u_2^{n+1}(r, \theta_-) &= \lambda_2^n(r)\,. \end{array}\right.$$

and

$$\begin{array}{rl} \lambda_1^{n+1}(r) &= -\lambda_2^n(r) + \Big(\tilde\beta_1(r) + \tilde\beta_2(r) - \partial_r(\frac{[\tilde\alpha_1(r) + \tilde\alpha_2(r)]}{2}\partial_r)\Big) u_2^{n+1}(r, \theta_-) \\ \lambda_2^{n+1}(r) &= -\lambda_1^n(r) + \Big(\tilde\beta_1(r) + \tilde\beta_2(r) - \partial_r(\frac{[\tilde\alpha_1(r) + \tilde\alpha_2(r)]}{2}\partial_r)\Big) u_1^{n+1}(r, \theta_-) \end{array} \tag{12}$$

3.3 Discrete problem

This subsection is concerned with the finite element implementation of the interface conditions along the interface. The numerical computations with the FreeFem++ software consist in introducing the problem to be solved in each subdomain with its weak formulation. The

variational formulation of the problem for each subdomain with interface conditions (5) is given by

$$\int_{\Omega_i} \eta\, u_i^{n+1} v_i + \int_{\Omega_i} \nabla u_i^{n+1} \nabla v_i + \int_0^\infty \tilde{\beta}_i(r)(u_i^{n+1} v_i)(r,\theta_-) + \int_0^\infty \frac{\tilde{\alpha}_i(r)}{2}(\partial_r u_i^{n+1} \partial_r v_i)(r,\theta_-) = \int_{\Omega_i} f v_i + \int_0^\infty \lambda_i^n(r) v_i(r,\theta_-)\,;\, i \in \{1,2\}\,.$$

Formula (12) is also introduced in a weak form. All variational formulations are discretized by a P1-Lagrange finite element method. This leads to a matrix form of the algorithm:

$$\begin{aligned} \tilde{K_1} u_1^{n+1} &= f + B_1^T \lambda_1^n \\ \tilde{K_2} u_2^{n+1} &= f + B_2^T \lambda_2^n \\ M_\Gamma \lambda_1^{n+1} &= -M_\Gamma \lambda_2^n + (M_{\tilde{\beta}_1,\Gamma} + M_{\tilde{\beta}_2,\Gamma} + K_{\tilde{\alpha}_1,\Gamma} + K_{\tilde{\alpha}_2,\Gamma}) B_2 u_2^{n+1} \\ M_\Gamma \lambda_2^{n+1} &= -M_\Gamma \lambda_1^n + (M_{\tilde{\beta}_1,\Gamma} + M_{\tilde{\beta}_2,\Gamma} + K_{\tilde{\alpha}_1,\Gamma} + K_{\tilde{\alpha}_2,\Gamma}) B_1 u_1^{n+1} \end{aligned} \tag{13}$$

where $\lambda_1, \lambda_2, u_1$ and u_2 denote the degrees of freedom of the finite element functions approximating the solution of the continuous problem, with the same names. The matrices B_1 and B_2 are the restriction operators (entries are one or zero) corresponding to trace operators of the domains Ω_1 and Ω_2 along the interface $\{\theta = \theta_-\}$. The matrices $\tilde{K_1}$ and $\tilde{K_2}$ arise from the discretization of the Laplace subproblems with the interface conditions (5),

$$\tilde{K_j} = \eta M_j + K_j + B_j^T (M_{\tilde{\beta}_j,\Gamma} + K_{\tilde{\alpha}_j,\Gamma}) B_j, \forall j = 1,2. \tag{14}$$

Here K_1 and K_2 are the subdomain stiffness matrices, M_1 and M_2 are the subdomain mass matrices, M_Γ and $M_{\tilde{\beta}_j,\Gamma}$ are the interface mass matrices, and $K_{\tilde{\alpha}_j,\Gamma}$ is the interface stiffness matrix,

$$\begin{aligned} (M_\Gamma)_{ij} &= \int_0^\infty (\phi_i \phi_j)(r,\theta_-)\; dr, \\ (M_{\tilde{\beta}_k,\Gamma})_{ij} &= \int_0^\infty \tilde{\beta}_k(r)(\phi_i \phi_j)(r,\theta_-)\; dr, \\ (K_{\tilde{\alpha}_k,\Gamma})_{ij} &= \int_0^\infty \frac{\tilde{\alpha}_k(r)}{2}(\partial_r \phi_i \partial_r \phi_j)(r,\theta_-)\; dr. \end{aligned}$$

The functions ϕ_i and ϕ_j are the basis functions associated with the degrees of freedom i and j along the interface $\{\theta = \theta-\}$.

3.4 Refined mesh around the corner

The effect of singularities associated with corners on domain decomposition methods occur when the discretization is fine enough. In order to show such effects without increasing excessively the numerical cost, a refinement of the mesh around the corner associated with the natural singularities of the global boundary value problem in Ω is introduced.

The specific mesh refinement which will be used is the one provided by [24] for the Dirichlet or Neumann problem on $\Omega = \mathbb{R}_+^* \times (\theta_0, \theta_+)$. Set $\omega = \theta_+ - \theta_0$ and assume that the right-hand side f of the problem

$$(\eta - \Delta)u = f \text{ in } \Omega, \quad u = 0 \text{ on } \partial\Omega \tag{15}$$

lies in the Sobolev space $H^m(\Omega)$, $m \in \mathbb{N}$. The theoretical result of [24] say that the solution u belongs to the weighted Sobolev space

$$W_\Psi^{m,2} = \{v \in \mathcal{D}'(\Omega) \text{ such that } \Psi\partial^j v \in L^2(\Omega), 0 \leq |j| \leq m\},$$

where the weight $\Psi(x)$ equals $|x|^\gamma = r^\gamma$ in the vicinity of the corner $r = 0$ and constant outside with:

$$\begin{array}{ll} \gamma & = 0 \text{ for } \omega < \frac{\pi}{m+1} \\ \gamma & > m + 1 - \frac{\pi}{\omega} \text{ if } \omega \geq \frac{\pi}{m+1}\,. \end{array}$$

This result also holds for the Neumann problem because Kondratiev theory provides the same singularity exponents $n\pi/\omega$, $n \in \mathbb{N}^*$ for the Dirichlet and Neumann problem. With such a choice of γ, a triangulation τ_h with generic mesh size $h > 0$ has to follow the next refinement rule in order to fit with the $W_\Psi^{m,2}$ regularity

- If K is a triangle of τ_h which does not touch $r = 0$, its diameter h_K satisfy the inequality $h_K \leq C\, h\, (\inf_K \Psi)^{\frac{1}{m+1}}$,
- If K is a triangle with a corner at $r = 0$, then $h_K \leq C h^{\frac{m+1}{m+1-\gamma}}$.

In the discretization for the Dirichlet and Neumann problem on Ω without any domain decomposition, such a refined mesh provides a good error control, similar to the one obtained for a uniform grid when there is no corner (see [24]). Although some numerical cases are presented with an interior artificial corner in $\Omega = (\mathbb{R}_+^* \times S^1) \cup \{O\}$, $(\omega = 2\pi)$, the same

simple refinement rule will be followed in all cases in order to have an accurate presentation of the singularity effects in domain decomposition. While doing so, it will be checked that the refinement process does not bring any other artificial numerical effects.

4 Numerical Experiments

4.1 Generalities

The theoretical approach presented in [4] consisted in determining the "best pairs" $(\alpha_\pm, \beta_\pm)$ from necessary conditions coming from an asymptotic analysis and then hope that in practice this choice improves significantly the speed of convergence. After recalling the results of this theoretical optimization, we present the numerical tests. The optimal choice of the pairs $(\alpha_\pm, \beta_\pm)$ is done for every subdomain Ω_j, $j = 1, \ldots, N$, by matching the singularities of the subdomain problem with well prepared data, which means with the expected singularities of the global problem in Ω. We already know from the theoretical analysis that two ways have to be considered for every subdomain Ω_j, $j = 1, \ldots, N$:

1. choose the coefficients $(\alpha_\pm, \beta_\pm)$ so that the first artificial singularity is canceled for well prepared data;

2. choose the pairs $(\alpha_\pm, \beta_\pm)$ so that the first artificial singularity has the highest possible exponent.

It is also known that the first approach does not admit a solution in all cases, depending on the total angle $\theta_+ - \theta_0$ of Ω and on the angle of the subdomain Ω_j. The second approach which will also be tested when necessary, is less efficient in agreement with the theoretical prediction.

Two possible types of corners, generated by the domain decomposition methods, were already mentioned in Subsection 3.1: There are corners which are in the interior of the global domain and other corners which are on the edge of the global domain. The treatment of these two categories of corners is slightly different and depends also on the type of boundary condition. For the corners in the interior of the global domain or on the boundary of the global domain with Neumann condition the coefficient $\beta_\pm$ has to be 0 in order to make possible a non vanishing value $u(O) \neq 0$. Meanwhile $\beta_\pm \neq 0$ is possible when the corner is

on the edge of the global domain with Dirichlet condition. Both cases will be presented in our numerical results.

When there are two coefficients, i.e. $\beta_\pm \neq 0$, a first relation between them is associated with the mesh discretization

$$\min\left\{\frac{\alpha_{opt}}{\alpha_\pm}, \frac{\beta_\pm}{\beta_{opt}}\right\} = \Phi(h) \tag{16}$$

where h is the general mesh size of the discretization and the length $\Phi(h)$ corresponds to the size of 3 possibly refined meshes. This equation ensures that the modification around the corner of the interface boundary conditions is numerically effective by involving a non zero number of meshes.

In our comparison of numerical methods, we shall use the terminology

1. **CICC** for the interface conditions (4) with constant coefficients $(\alpha_{opt}, \beta_{opt})$ up to the corner.

2. **COC** for the new interface condition (5)(6) with optimized coefficients at the corner $(\alpha_\pm, \beta_\pm)$.

Unlike the theoretical analysis and presentation, the domain Ω is bounded and will be specified in every case. This global domain Ω will be split into two or three subdomains.

The convergence will be tested and the logarithmic convergence curve will be plotted with the norm

$$|e|_1 = \Big(\int_\Omega |\nabla e|^2(x)dx\Big)^{1/2}$$

but the 3D plot of the error $|e(x)|$ will be presented with a reference to the L^∞-norm

$$|e|_\infty = \|e\|_{L^\infty(\Omega)} \ .$$

The right-hand side f is taken constant and equal to 1 in the whole domain Ω. It is used only at the initialization step: The starting subdomain solutions u_i^0 are computed by solving the subdomain problems like (10) and (11) with vanishing right-hand sides in the boundary conditions.

Practically the error function e^n at step n is computed as $u^N - u^n$ where u^n is the result after n iterations of the domain decomposition algorithm and N is large enough so that u^N is much closer to the (discrete) solution u^∞ than the numerical tolerance $\varepsilon = 10^{-6}$.

Finally all our numerical computations were done with the free finite element software FreeFem++ [9].

4.2 The L-shaped domain with Dirichlet boundary condition

We consider here the simple case of an L-shaped domain with $\theta_0 = -\frac{3\pi}{2}, \theta_+ = 0, \theta_- \in (-\pi, -\pi/2)$. Of course a numerical treatment requires a bounded domain $\overline{\Omega}$. The L-shaped domain Ω is thus made with two rectangles adjacent to the quarter of a disc and Dirichlet boundary conditions are set on $\partial\Omega$. This shape was chosen in order to vary the interface angle $\theta_- \in (-\pi, -\pi/2)$ without changing the nature of the new artificial corner opposite to the corner $r = 0$ of interest. Here only the case $\theta_- = -3\pi/4$ will be presented with other more relevant discussions about the numerical parameters.

Consider the homogeneous Dirichlet problem

$$(\eta - \Delta)u = f \quad u\big|_{\partial\Omega} = 0\,. \tag{17}$$

The domain $\Omega \subset \mathbb{R}_+^* \times (\theta_0, \theta_+)$ in polar coordinates is decomposed into

$$\Omega_1 = \Omega \cap \big(\mathbb{R}_+^* \times (\theta_-, \theta_+)\big) \quad \text{and} \quad \Omega_2 = \Omega \cap \big(\mathbb{R}_+^* \times (\theta_0, \theta_-)\big)\,,$$

with $\theta_0 < \theta_- < \theta_+$. The boundary problem solved by the error $e_1^{n+1} = u_1^{n+1} - u$ reads

$$\left\{\begin{array}{rl} \Big(\eta - \frac{1}{r^2}((r\partial_r)^2 + \partial_\theta^2)\Big)e_1^{n+1}(r,\theta) & = 0 \text{ in } \Omega_1 \\ e_1^{n+1}\big|_{\partial\Omega\cap\partial\Omega_1} & = 0 \\ \Big(-\frac{1}{r}\partial_\theta + \tilde{\beta}_-(r) - \frac{1}{2}\partial_r(\tilde{\alpha}_-(r)\partial_r)\Big)e_1^{n+1}(r,\theta_-) & = g_-(r) \end{array}\right. \tag{18}$$

with $g_-(r) = \Big(-\frac{1}{r}\partial_\theta + \tilde{\beta}_-(r) - \frac{1}{2}\partial_r(\tilde{\alpha}_-(r)\partial_r)\Big)e_2^n(r,\theta_-)$. The boundary $\{\theta = \theta_+\} \cap \Omega$ is included here in $\partial\Omega \cap \partial\Omega_1$ and a similar boundary value problem is written for Ω_2.

For general angles, $0 < \theta_- - \theta_0 < \theta_+ - \theta_0 < 2\pi$, the theoretical analysis of [4] provides the relation for the optimal pair (α_-, β_-)

$$-\beta_- + \frac{\alpha_-}{2x_0^2} = \frac{1}{x_0\tan(\frac{\pi x}{x_0})}, \quad x_0 = \frac{\theta_+ - \theta_0}{\pi}\,, \quad x = \frac{\theta_+ - \theta_-}{\pi}\,. \tag{19}$$

Here with $\theta_+ = 0$, $\theta_0 = -3\pi/2$ and $\theta_- = -3\pi/4$ it becomes

$$\frac{\beta_-}{\alpha_-} = \frac{2}{9}\,. \tag{20}$$

Keep in mind that this relationship has to be combined with (16) which ensures that the coefficients (α_-, β_-) are numerically effective on 3 (for these tests) meshes.

The optimality of the relationship (20) is checked numerically while numerical tests with three types of grids show :

1. The artificial singularities have a bad effect on the algorithm only for accurate calculations, i.e. after a certain number of iterations and with a refined mesh around the corner.

2. The mesh refinement does not induce any other artificial numerical effect.

4.2.1 Refined mesh around the corner

We use a uniform grid everywhere except at the corner $r = 0$. The right-hand side $\Phi(h)$ in the matching relationship (16) corresponds to three refined meshes of the discretized domain. The domain decomposition algorithm is tested with various ratios β_-/α_- in order to check that (20) is optimal (see Table 1). We recall the abbreviation **COC** for the optimal pair (α_-, β_-) and a comparison will be made with the **CICC** case (constant coefficients along the interface). With **CICC**, 15 iterations are necessary in order to reach $|e^n|_1 \leq 10^{-6}$ instead of 9 with **COC** and the curve of $\log_{10} |e^n|_1$ with respect to n in Figure 1 shows the improvement brought by **COC**.

$\frac{\beta_-}{\alpha_-}$	0.05	0.1	2/9	1	2	5	10
Iteration count	16	13	9	12	24	59	116

Table 1: Refined mesh around the corner: Number of iterations for different values of $\frac{\beta_-}{\alpha_-}$, with $|e|_1 < 10^{-6}$.

The 3D plots of the error $e^n(x)$ is even more convincing. The Figures 2,...,5 show that the error has a very stiff peak in the vicinity of the corner if nothing is done at the corner (**CICC**). Meanwhile, the error is quite uniformly spread with the **COC** method (see Figures 6,...,9).

4.2.2 Case without refinement

The previous effects cannot be distinguished when the grid is too coarse. With a uniform grid with the same interior mesh size $h > 0$ as before and with $\Phi(h) = 3h$ in (16), 9 iterations

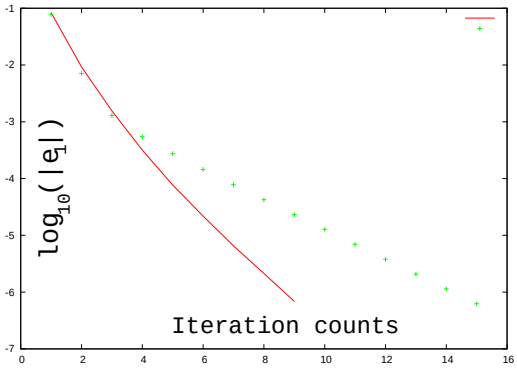

Figure 1: L-shaped domain with refinement at the corner: **COC**(solid line), **CICC** (dotted line)

are necessary with **COC** in order to reach $|e^n|_1 \leq 10^{-6}$ while only 10 iterations suffices with **CICC**.

The Figures 10 and 11 show the error $|e_1^7(x)|$ respectively with **CICC** and **COC**, without a difference comparable to the one in 4.2.1.

4.2.3 Case with refinement at the corner and in the middle of the edge

This last test ensures that the phenomenon observed in 4.2.1 is not an artefact of the mesh refinement around the corner. The grid is refined at the corner and in the middle of the edge without showing any special behaviour due to this additional refinement.
Like in case 4.2.1, the relation $\frac{\beta_-}{\alpha_-} = \frac{2}{9}$ is optimal according to the next table. Moreover,

$\frac{\beta_-}{\alpha_-}$	0.05	0.1	2/9	1	2	5	10
Iteration count	15	13	9	12	23	56	111

Table 2: L-shaped domain with refinement at the corner and the edge, with $|e|_1 < 10^{-6}$.

with **CICC**, 14 iterations are necessary instead of 9 with **COC** .
The Figures 12 and 13 presents the error $|e_1(x)|$ for **CICC** while the Figures 14 and 15 corresponds to **COC**. No important difference with case 4.2.1 arises.

4.3 Interior artificial corner

The domain Ω is the unit disc of $\mathbb{R}^2$, $\Omega = \{(r\cos(\theta), r\sin(\theta)), r \in [0,1], \theta \in [0, 2\pi)\}$ and we consider the homogeneous Dirichlet problem

$$(\eta - \Delta)u = f \text{ in } \Omega, \quad u = 0 \text{ on } \partial\Omega\,. \tag{21}$$

The domain Ω in polar coordinates is decomposed into two or three sectorial subdomains with vertex at $r = 0$. Again, we focus on $\Omega_1 = [0,1] \times (\theta_-, \theta_+)$ while the other subdomains Ω_2 and possibly Ω_3 are treated similarly. The boundary problem (21) with the selected interface conditions (5) solved by the error $e_1^{n+1} = u_1^{n+1} - u$ reads

$$\left\{\begin{array}{rl} \Big(\eta - \frac{1}{r^2}((r\partial_r)^2 + \partial_\theta^2)\Big) e_1^{n+1}(r,\theta) & = 0 \text{ in } \Omega_1 \\ e_1^{n+1}\big|_{\partial\Omega\cap\partial\Omega_1} & = 0 \\ \Big(\frac{1}{r}\partial_\theta + \frac{1}{2}\partial_r(\tilde{\alpha}_-(r)\partial_r)\Big) e_1^{n+1}(r,\theta_-) & = g_-(r) \\ \Big(\frac{1}{r}\partial_\theta - \frac{1}{2}\partial_r(\tilde{\alpha}_+(r)\partial_r)\Big) e_1^{n+1}(r,\theta_+) & = g_+(r) \end{array}\right. \tag{22}$$

where $g_-(r) = \Big(\frac{1}{r}\partial_\theta + \frac{1}{2}\partial_r(\tilde{\alpha}_-(r)\partial_r)\Big) e_2^n(r,\theta_- + 2\pi)$ and $g_+(r) = \Big(\frac{1}{r}\partial_\theta - \frac{1}{2}\partial_r(\tilde{\alpha}_+(r)\partial_r)\Big) e_2^n(r,\theta_+)$. Here the equality $\beta_\pm = 0$ is necessary because the solution u has in general a non zero value at $r = 0$ (see Subsection 3.1). Only the coefficients $\alpha_\pm$ can be used and the equation (16) is not necessary. The condition $\alpha_{opt}/\alpha_\pm \geq \Phi(h)$ is checked afterwards.

The theoretical analysis of [4] says that the optimal choice of the pair (α_+, α_-) is given by

$$\alpha_+ = \alpha_- = \alpha_1 = \frac{2}{\tan(\frac{\pi x(\Omega_1)}{2})}\,, \quad x(\Omega_1) = \frac{\theta_+ - \theta_-}{\pi}\,. \tag{23}$$

Hence the coefficient $\alpha_\pm = \alpha_1$ is non negative only when the sector Ω_1 is convex

$$\theta_+ - \theta_- \in (0,\pi), \qquad x(\Omega_1) \in (0,1)\,.$$

When the disc Ω is decomposed into 2 subdomains, one of them must be non convex. Assume $x(\Omega_1) < 1$ and $x(\Omega_2) > 1$. The first strategy can be applied in Ω_1 with the optimal choice $\alpha_\pm = \alpha_1$ while the coefficient $\alpha_\pm = 0$ or chosen very small in Ω_2 pushes the first artificial singularity as far as possible (second strategy). With this choice the expansion of the artificial singularities around $r = 0$ has the order $O(r^{\min(t_2(\Omega_1), t_1(\Omega_2))})$ where the exponents $t_j(\Omega_i)$ satisfy $0 < t_1(\Omega_i) < t_2(\Omega_j)$.

Convex sectors can be obtained with a decomposition into three convex subdomains. Then the optimal choice $\alpha_\pm = \alpha_i$ can be done in every subdomain so that the first artificial singularity $O(r^{\min(t_2(\Omega_1), t_2(\Omega_2), t_2(\Omega_3))})$ suggests a better convergence (see [4]).

Both cases are numerically tested below. For all the presented numerical results it was checked that the matching radius $\frac{\alpha_{opt}}{\alpha_i}$ in domain Ω_i was larger than three meshes of the possibly refined grid.

4.3.1 Decomposition into three subdomains

Here the disc is decomposed into three isometric sectors with angle $\theta_+ - \theta_- = \frac{2\pi}{3}$ so that the optimal coefficients equal

$$\alpha_1 = \alpha_2 = \alpha_3 = \frac{2}{\tan \pi/3} = \frac{2}{\sqrt{3}}\,.$$

With a refined mesh around the corner, the optimality of the coefficient is confirmed by the next Table. In this configuration the **COC** requires 11 iterations while 20 iterations are

$\alpha \tan(\frac{\pi x}{2})$	30	20	2	0.15	0.1	0.02
Iteration count	16	14	11	34	40	62

Table 3: Disc decomposed into 3 subdomains with refinement at the corner, $|e|_1 < 10^{-6}$.

necessary with the **CICC**, see Figure 16.

The 3D plots of the error after 10 iterations shows again a stiff peak for the **CICC** method and a uniformly spread error for the **COC** method (see Figures 17 and 18)
Like for the L-shaped domain, some computations were done with a uniform grid and an artificial refinement in the middle of the edge.

1. Uniform grid: The **COC** and **CICC** both require 11 iterations in order to get $|e|_1 < 10^{-6}$ (3D plots in Figures 19 and 20)

2. Refined mesh in the edge and at the corner: With **CICC** 15 iterations are necessary instead of 12 with **COC**, for $|e|_1 < 10^{-6}$ (3D plots in Figures 21 and 22).

4.3.2 Decomposition into two subdomains

Here the disc is decomposed into two sectors with angles $\frac{2\pi}{3}$ and $\frac{4\pi}{3}$. In the non convex subdomain Ω_2 with angle $\frac{4\pi}{3}$ the choice of $\alpha_\pm = 0$ is done by taking $\tilde{\alpha}_\pm(r)$ proportional to r^2 on 5 meshes of the grid close to the corner. In the convex subdomain Ω_1 with angle $\frac{2\pi}{3}$, we take $\alpha_1 = \frac{2}{\sqrt{3}}$ and we checked that the matching point was further than 4 meshes.
The comparison between the **CICC** and **COC** methods gave:

In the decomposition into two subdomains, the improvement of the convergence is not so obvious. This method is less efficient than the decomposition into three convex sectors. Only a slight improvement is brought by the **COC** method as shown also in the 3D plots of $|e(x)|$ in Figures 23 and 24.

	COC	CICC
Iteration count	20	22

Table 4: Disc with two subdomains. Refinement at the corner. $|e|_1 < 10^{-6}$.

	COC	CICC
Iteration count	20	21

Table 5: Disc with two subdomains. Refinement at the corner and in the edge. $|e|_1 < 10^{-6}$.

4.4 The Neumann problem

Here we consider the sectorial domain $\Omega = \{(r\cos(\theta), r\sin(\theta)), r > 0, \theta_0 < \theta < \theta_+\}$, with $\theta_+ - \theta_0 \in (0, 2\pi)$. Consider the mixed problem

$$(\eta - \Delta)u = f \quad \partial_n u\big|_{\theta=\theta_0} \equiv 0 \quad \partial_n u\big|_{\theta=\theta_+} \equiv 0 \quad u\big|_{r=1} \equiv 0\,. \tag{24}$$

The decomposition is made into 2 or 3 subdomains and we write $\Omega_1 = \left(\mathbb{R}_+^* \times (\theta_-, \theta_+)\right) \cap \Omega$. In order to have a well posed problem in Ω_1 and Ω_2 which permits non null values at the corner, we must take $\beta_- = 0$ like in the interior corner problem (with the same consequences for the numerical implementations).

The boundary problem (24) in Ω_1 with the interface conditions (5) solved by the error $e_1^{n+1} = u_1^{n+1} - u$ reads

$$\left\{\begin{array}{rl} \left(\eta - \frac{1}{r^2}((r\partial_r)^2 + \partial_\theta^2)\right)e_1^{n+1}(r,\theta) & = 0 \text{ in } \Omega_1 \\ e_1^{n+1}(1,\theta) & = 0 \\ \partial_\theta e_1^{n+1}(r,\theta_+) & = 0 \\ \left(\frac{1}{r}\partial_\theta + \frac{1}{2}\partial_r(\tilde{\alpha}_-(r)\partial_r)\right)e_1^{n+1}(r,\theta_-) & = g_-(r) \end{array}\right. \tag{25}$$

where $g_-(r) = \left(\frac{1}{r}\partial_\theta + \frac{1}{2}\partial_r(\tilde{\alpha}_-(r)\partial_r)\right)e_2^n(r,\theta_-)$.

In the subdomain Ω_1 the optimal value of α_- is given by

$$\alpha_- = -2x_0\tan(\frac{\pi x}{x_0})\,, \quad x = \frac{\theta_+ - \theta_-}{\pi},\ x_0 = \frac{\theta_+ - \theta_0}{\pi}\,. \tag{26}$$

In our case with $x_0 = \frac{3}{2}$ it can be non negative only with the condition

$$\frac{x_0}{2} < x \leq x_0, \text{ i.e. } \theta_+ - \theta_- > \frac{3\pi}{4}$$

	COC	CICC
Iteration count	13	13

Table 6: Disc with two subdomains. Uniform grid. $|e|_1 < 10^{-6}$.

which plays the same role as the convexity condition in the interior corner problem. The two strategies will be tested:

1. Decomposition into two subdomains with $\theta_+ - \theta- > 3\pi/4$. In the second subdomain Ω_2 with angle less than $3\pi/4$, the choice $\alpha_- = 0$ (implemented with an $O(r^2)$ coefficient close to the corner) pushes the exponent $t_1(\Omega_2)$ as far as possible.

2. Decomposition into three subdomains. The choice $\alpha_- = 0$ has to be done in Ω_1 and a symmetric choice has to be done in Ω_3. The case of the middle subdomain Ω_2 will be discussed further.

4.4.1 Decomposition into two subdomains

The opening angle of Ω_1 is $\frac{6\pi}{5} > \frac{3\pi}{4}$ and the one of Ω_2 equals $\frac{3\pi}{10} < \frac{3\pi}{4}$. The comparison of the **COC** and **CICC** methods for the three types of grids is given in the next tables.

	COC	**CICC**
Iteration count	13	26

Table 7: L-shaped with two subdomains. Refinement at the corner. $|e|_1 < 10^{-6}$.

	COC	**CICC**
Iteration count	14	26

Table 8: L-shaped with two subdomains. Refinement at the corner and in the edge. $|e|_1 < 10^{-6}$.

	COC	**CICC**
Iteration count	14	14

Table 9: L-shaped with two subdomains. Uniform grid. $|e|_1 < 10^{-6}$.

The convergence curve with a refined mesh at the corner is shown in Figure 25.

The 3D plots of the error $|e(x)|$ with a refined mesh around the corner in Figures 26 and 27 also show that this approach kills the singularity in Ω_1.

4.4.2 Decomposition into three subdomains

The three domains are chosen with the same opening angle $\pi/2$. For the subdomains Ω_1 and Ω_3 the choice $\alpha_\pm = 0$ is implemented by taking $\tilde{\alpha}_\pm(r)$ proportional to r^2 on 5 meshes of the grid close to the corner.

The middle subdomain Ω_2 with two interfaces, has to be treated like in the interior corner problem. Nevertheless the well-prepared data associated with the global problem in Ω lead to the impossibility of the optimization of $\alpha_\pm(\Omega_2)$. The choice $\alpha_\pm = 0$ implemented by truncation has to be done also in Ω_2.

The computations were done with a refined mesh around the corner and also with an additional refinement in the middle of the edge. With **CICC** 13 iterations were necessary in order to get an error $|e|_1$ smaller than 10^{-6}, instead of 12 iterations with **COC**, in both cases.

With refinement only at the corner a slight improvement appears on the 3D plot of $|e(x)|$ for the **COC** method (no peak in Figure 29 in comparison with Figure 28).

5 Conclusion

All the numerical experiments show that the implementation of **COC** methods improves the behaviour of the error e^n in the decomposition algorithms. Even when the optimized coefficients do not exist and when the second less efficient strategy (of pushing the first artificial singularity as far as possible) has to be chosen, the symptomatic peak of the error function $|e(x)|$ is reduced. The effect on the convergence curve is significant when the optimized pairs $(\alpha_\pm, \beta_\pm)$ exist and can be implemented. The numerical experiments where the ratio $\frac{\beta_\pm}{\alpha_\pm}$ is changed also show that this choice is really the optimal one numerically. Finally the conclusion of the experiments on the interior artificial corner and on the Neumann problem in the L-shaped sector show that the more the first strategy (with optimal coefficients) is applied, the better the convergence is.

References

[1] C. Carlenzoli, A. Quarteroni. Adaptive domain decomposition methods for advection-diffusion problems, The IMA Volumes in Mathematics and its Applications, Vol. 75, Springer Verlag, 1995, pp. 165-186.

[2] T.F. Chan, T.P. Mathew. Domain decomposition algorithms.
In Acta Numerica 1994, pages 61-143.Cambridge University Press, 1994.

[3] P. Charton, F. Nataf, F. Rogier. Méthode de décomposition de domaine pour l'équation d'advection-diffusion, C. R. Acad. Sci. Paris,t. 313, serie I, 1991, pp. 623-626.

[4] C. Chniti, F. Nataf, F. Nier. Improved interface condition for 2D domain decomposition with corner : a theoretical determination.
Preprint IRMAR 06-02. (http://has.ccsd.cnrs.fr)

[5] M. Dauge. Lecture Notes in Mathematics 1341. Elliptic Boundary Value Problems on Corner Domains. March 5th, 1988.

[6] B. Després. Domain decomposition methods and the Helmholtz problem, Mathematical and Numerical aspects of wave propagation phenomena, SIAM. 1991, pp. 44-52.

[7] B. Engquist, A. Majda. Radiation Boundary Conditions for Acoustic and Elastic Wave Calculations, Comm. on Pure and App. Math, Vol. 32, 1979, pp. 313-357.

[8] B. Engquist, A. Majda. Absorbing Boundary Conditions for the Numerical Simulation of Waves, MAth. Comp. 31 (139), 1977, pp. 629-651.

[9] FreeFem++, http:\\www.freefem.org

[10] P. Grisvard. Behavior of the solutions of an Elliptic Boundary Value Problem in a Polygonal or Polyhedral Domain.

[11] T. Hagstrom, R.P. Tewarson, A. Jazcilevich. Numerical Experiments on a Domain Decomposition Algorithm for Nonlinear Elliptic Boundary Value Problem, Appl. Math.Lett.1, n°3, 1988, pp.299-302.

[12] C. Japhet and F. Nataf. The best interface Conditions for domain decomposition methods : Absorbing boundary conditions. To appear in Artificial Boundary Conditions, with applications to computational Fluid Dynamics Problems' edited by L.Tourrette, Nova Science, 2000.

[13] V.A. Kondratiev. Boundary problems for elliptic equations in domains with conical or angular points. Trudi Mosk. Mat. Obsc, 16, 1996, 209-292.

[14] P.L. Lions. On the Schwarz Alternating Method I,
First Int.Symp.on Domain Decomposition Methods(R.Glowinski, G.H Golub, G.A. Meurant and J.Periaux,eds), SIAM (Philadelphia,PA), 1988.

[15] P.L. Lions. On the Schwarz Alternating Method III
A variant for Nonoverlapping Subdomains,Third Internationnal Symposium on Domain Decomposition Methods for Partial Differentiel Equations, SIAM, 1989, pp.202-223.

[16] F. Nataf. Etude et utilisation algorithmique des notions de condition à la limite artificielle et de factorisation. Cas de l'équation de convection-diffusion, Habiliation à diriger des recherches, Université Paris XIII, 1995.

[17] F. Nataf, F. Rogier. Factorisation of the convection diffusion operator and the Schwarz Algorithms, MAS, 5, n°1, 1995, pp. 67-93.

[18] F. Nataf, F. Rogier. Outflow Boundary Conditions and Domain Decomposition Method, Contemporary Mathematics, Vol.180, 1994, pp.289-293.

[19] F. Nataf, F. Rogier, E. de Sturler. Domain decomposition methods for fluid dynamics, In Sequeira A.(ed) Navier-stokes equations on related non linear analysis, pp.307-377. Plenum Press Corporation, 1995.

[20] F. Nataf, F. Nier. Convergence rate of some Domain Decomposition Methods for Overlapping and Nonoverlapping Subdomains, Numerische Mathematik, Vol.75, 1997, pp. 357-377.

[21] F. Nataf, F. Nier. Convergence of Domain Decomposition Methods via Semi-Classical Calculus. Commun in Partial Differenrial Equations, 23(5,6), 1998, pp. 1007-1059.

[22] F. Nier. Remarques sur les algorithmes de décomposition de domaines. In séminaire EDP-Ecole polytechnique 1998-99.

[23] A. Quarteroni, A. Valli.Domain decomposition methods for partial Differential Equations. Oxford Science Publications, 1999.

[24] G. Raugel. Résolution numérique par une méthode d'éléments finis du problème de Dirichlet pour le laplacien dans un polygone. C.R Acad. Sc. Paris, t.286(8 mai 1978), serie A, pp. 791-794.

[25] H.A. Schwarz. Über einen Grenzübergang durch alternierendes Verfahren, Vierteljahrsschrift der Naturforschenden Gesellschaft in Zürich Vol.15, may 1870, pp.272-286.

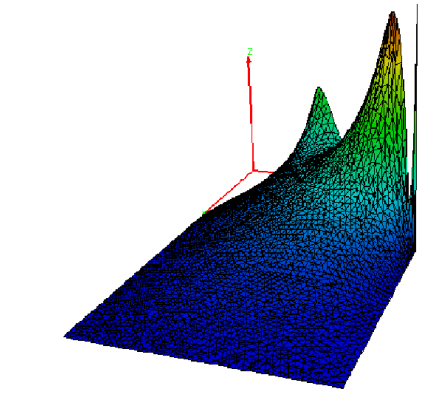

Figure 2: Error $|e_1^2(x)|$ with **CICC** after two iterations, with $|e^2|_\infty = 7.6 \times 10^{-4}$.

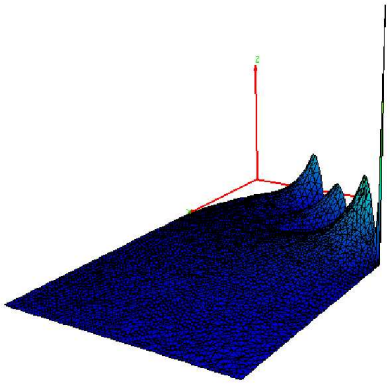

Figure 3: Error $|e_1^4(x)|$ with **CICC** after four iterations, with $|e^4|_\infty = 1.9 \times 10^{-4}$.

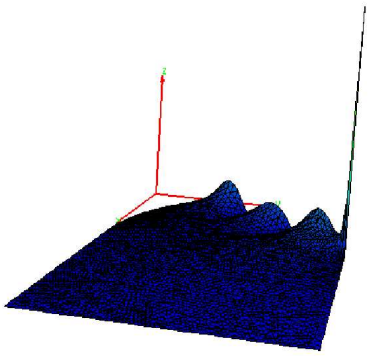

Figure 4: Error $|e_1^6(x)|$ with **CICC** after six iterations, with $|e^6|_\infty = 5.65 \times 10^{-5}$.

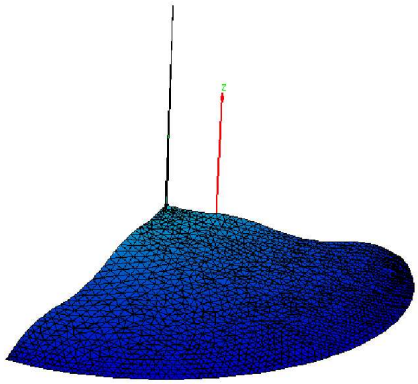

Figure 5: Error $|e_1^8(x)|$ with **CICC** after eight iterations, with $|e^8|_\infty = 1.66 \times 10^{-5}$.

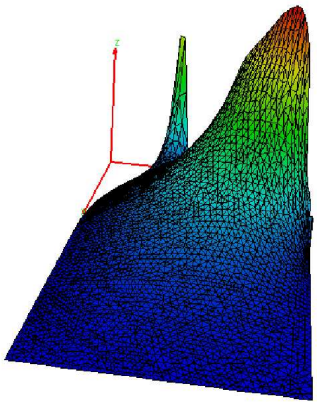

Figure 6: Error $|e_1^2(x)|$ with **COC** after two iterations, with $|e^2|_\infty = 10^{-3}$.

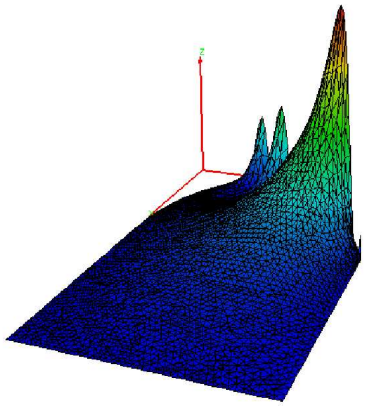

Figure 7: Error $|e_1^4(x)|$ with **COC** after four iterations, with $|e^4|_\infty = 6 \times 10^{-5}$.

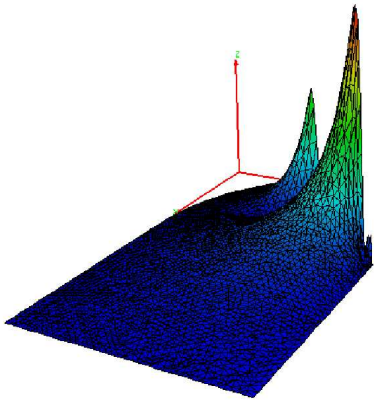

Figure 8: Error $|e_1^6(x)|$ with **COC** after six iterations, with $|e^6|_\infty = 5.2 \times 10^{-6}$.

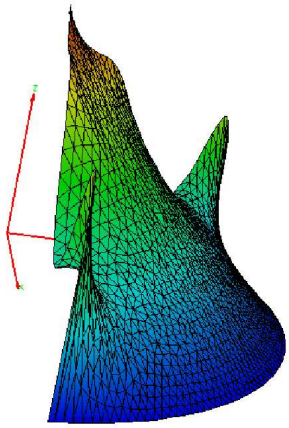

Figure 9: Error $|e_1^8(x)|$ with **COC** after eight iterations, with $|e^8|_\infty = 5.49 \times 10^{-7}$.

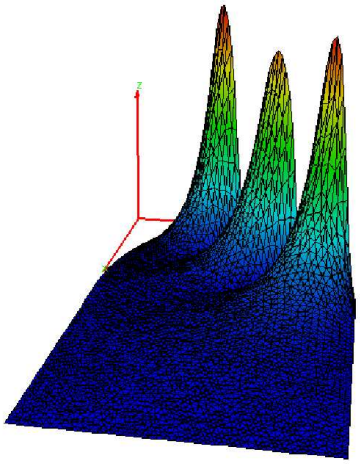

Figure 10: L-shaped domain without refinement, Error $|e_1^7(x)|$ with **CICC** after seven iterations with $|e^7|_\infty = 2.85 \times 10^{-6}$.

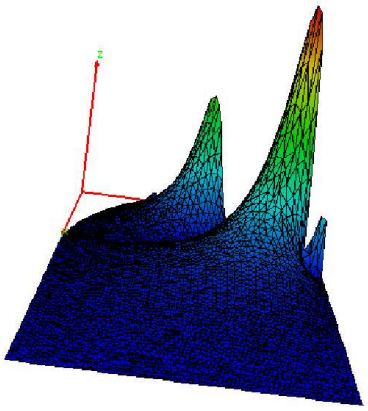

Figure 11: L-shaped domain without refinement, Error $|e_1^7(x)|$ with **COC** after seven iterations with $|e^7|_\infty = 1.72 \times 10^{-6}$.

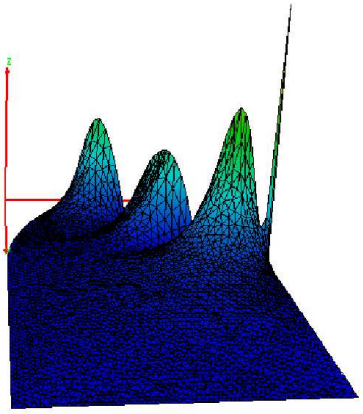

Figure 12: L-shaped domain, refinement at the corner and in the edge, Error $|e_1^5(x)|$ with **CICC** after five iterations, with $|e^5|_\infty = 1.55 \times 10^{-4}$.

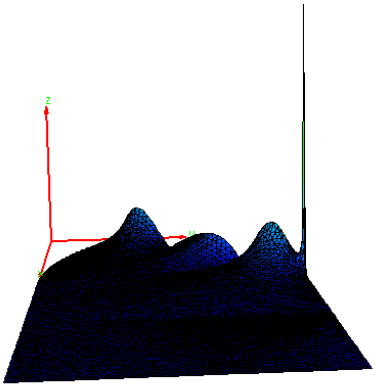

Figure 13: L-shaped domain, refinement at the corner and in the edge, Error $|e_1^9(x)|$ with **CICC** after nine iterations with $|e^9|_\infty = 1.18 \times 10^{-5}$.

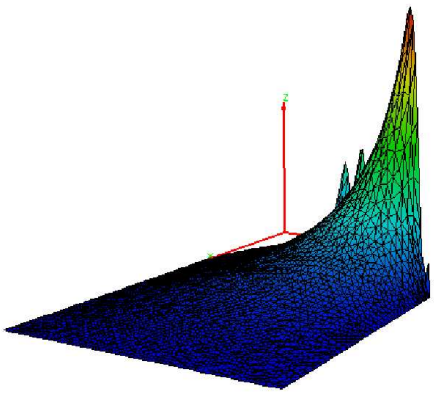

Figure 14: L-shaped domain, refinement at the corner and in the edge, Error $|e_1^5(x)|$ with **COC** after five iterations, with $|e^5|_\infty = 6.50 \times 10^{-5}$.

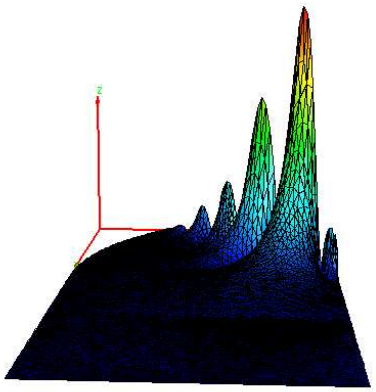

Figure 15: L-shaped domain, refinement at the corner and in the edge, Error $|e_1^9(x)|$ with **COC** after nine iterations with $|e^9|_\infty = 1.33 \times 10^{-6}$.

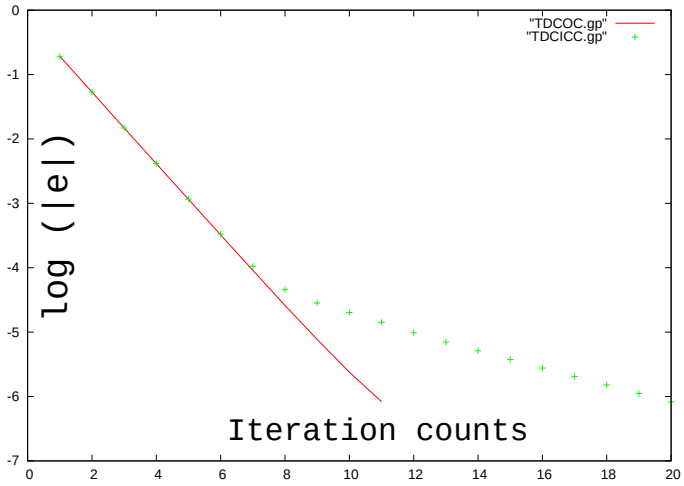

Figure 16: Disc decomposed into three subdomains with refinement at the corner: **COC**(solid line), **CICC** (dotted line) .

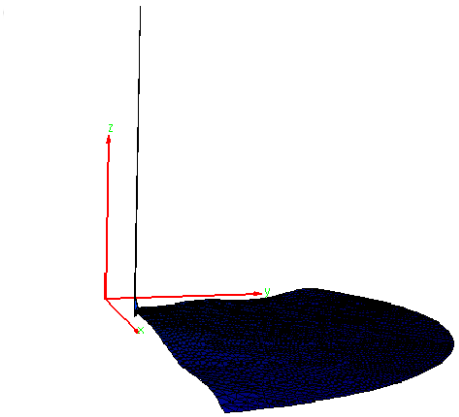

Figure 17: Disc decomposed into 3 subdomains. Refinement at the corner. Error $|e_1^{10}(x)|$ with **CICC** after ten iterations, with $|e^{10}|_\infty = 1.08 \times 10^{-5}$.

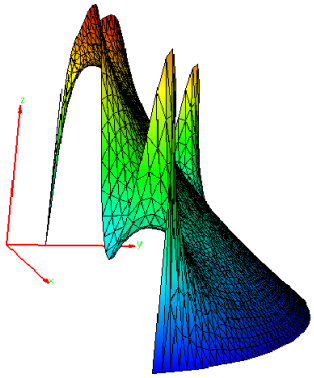

Figure 18: Disc decomposed into 3 subdomains. Refinement at the corner. Error $|e_1^{10}(x)|$ with **COC** after ten iterations, with $|e^{10}|_\infty = 4.22 \times 10^{-7}$.

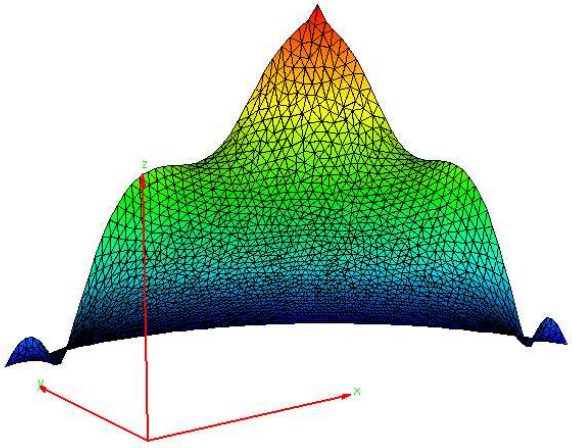

Figure 19: Disc decomposed into 3 subdomains. Uniform grid. Error $|e_1^{11}(x)|$ with **CICC** after eleven iteration with $|e^{11}|_\infty = 2.06 \times 10^{-6}$.

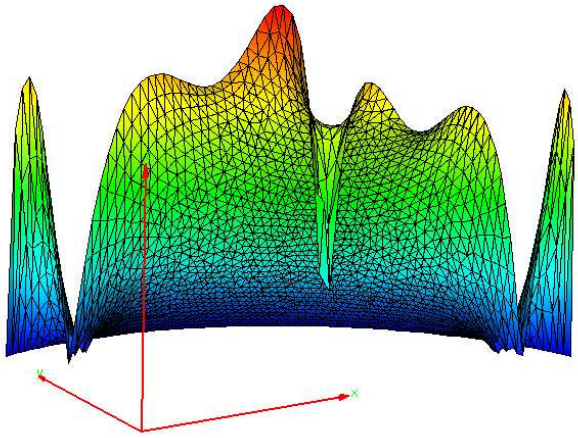

Figure 20: Disc decomposed into 3 subdomains. Uniform grid. Error $|e_1^{11}(x)|$ with **COC** after eleven iteration with $|e^{11}|_\infty = 1.36 \times 10^{-6}$.

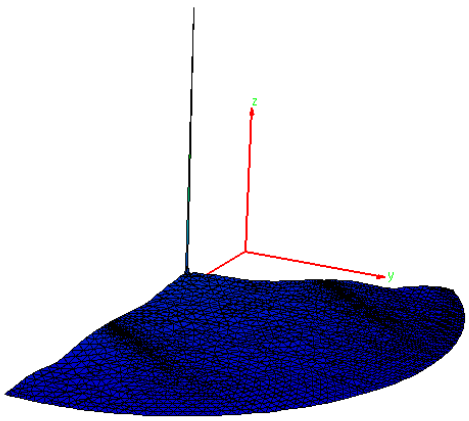

Figure 21: Disc decomposed into 3 subdomains. Refined mesh at the corner and in the edge. Error $|e_1^{11}(x)|$ with **CICC** after 11 iterations with $|e^{11}|_\infty = 3.57 \times 10^{-6}$.

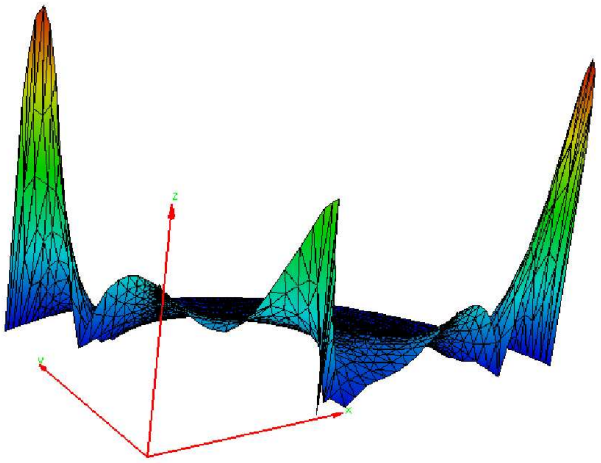

Figure 22: Disc decomposed into 3 subdomains. Refined mesh at the corner and in the edge. Error $|e_1^{11}(x)|$ with **COC** after 11 iterations with $|e^{11}|_\infty = 5.6 \times 10^{-7}$.

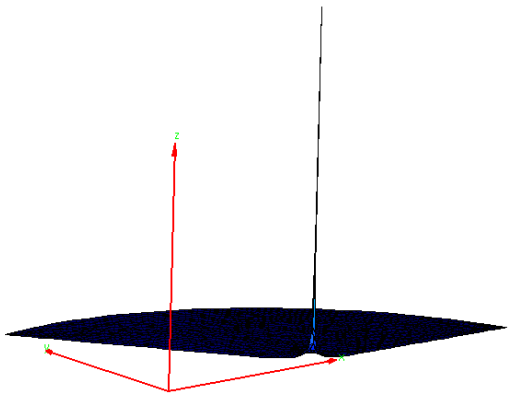

Figure 23: Disk with two subdomains. Refined mesh. Error $|e_1^{20}(x)|$ with **CICC** after twenty iterations with $|e^{20}|_\infty = 1.25 \times 10^{-6}$.

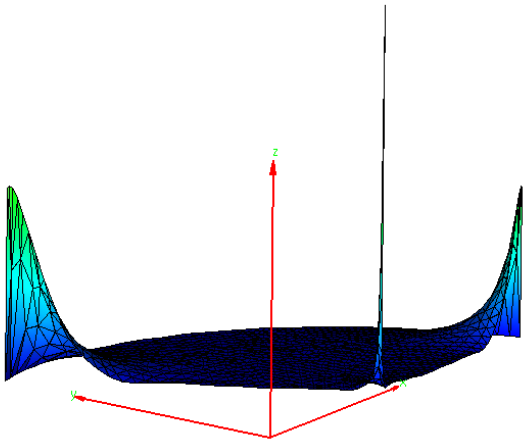

Figure 24: Disk with two subdomains. Refined mesh. Error $|e_1^{20}(x)|$ with **COC** after twenty iterations with $|e^{20}|_\infty = 6.64 \times 10^{-7}$.

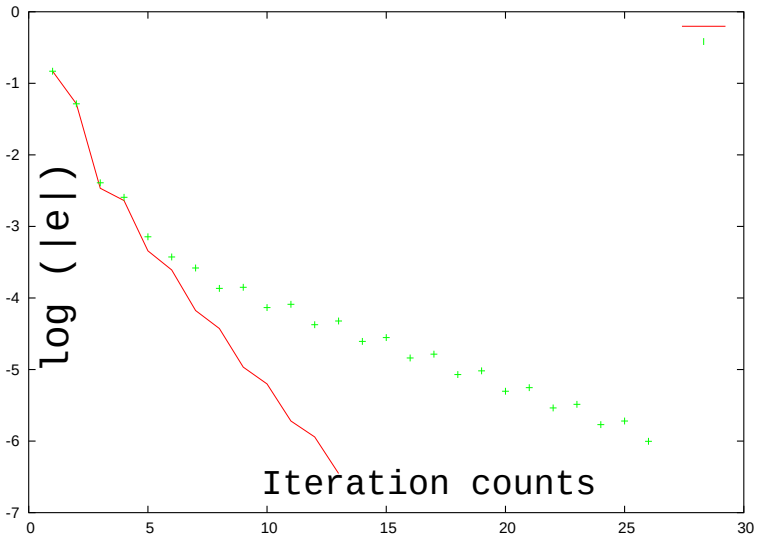

Figure 25: Neumann problem with refinement at the corner: **COC**(solid line), **CICC** (dotted line).

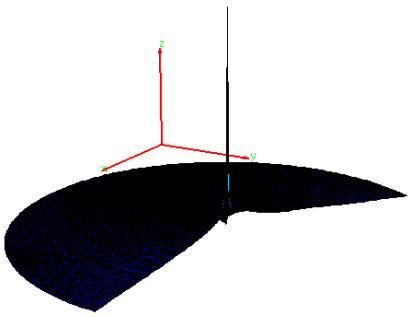

Figure 26: Refined mesh at the corner. Error $|e_1^{13}(x)|$ with **CICC** after 13 iterations, with $|e^{13}|_\infty = 2.13 \times 10^{-5}$.

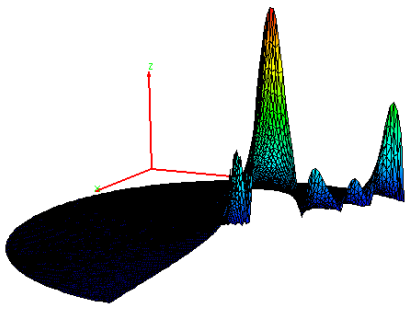

Figure 27: Refined mesh at the corner. Error $|e_1^{13}(x)|$ with **COC** after 13 iterations, with $|e^{13}|_\infty = 2.47 \times 10^{-7}$.

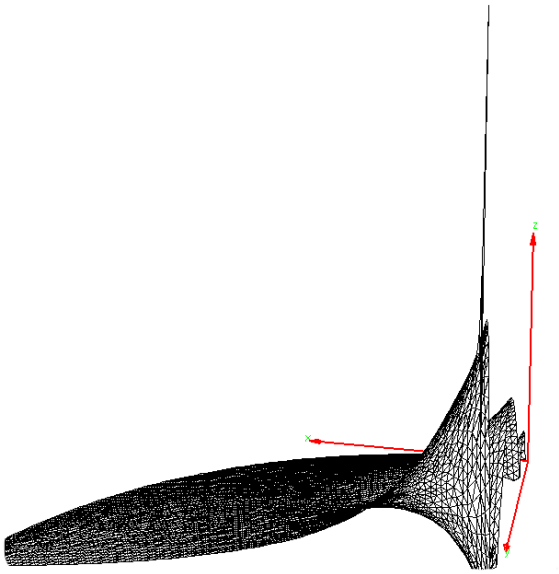

Figure 28: L-shaped decomposed into 3 subdomains. Refinement at the corner. Error $|e_1^{12}(x)|$ with **CICC** after 12 iterations, with $|e^{12}|_\infty = 1.51 \times 10^{-6}$.

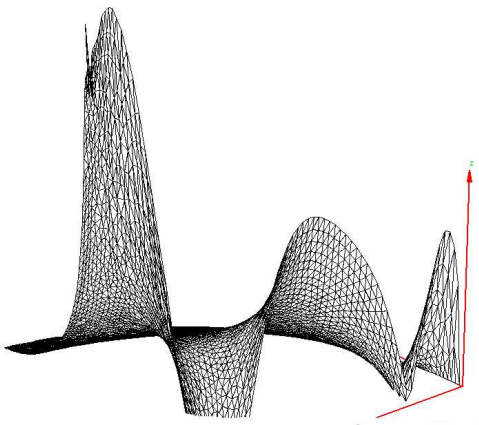

Figure 29: L-shaped decomposed into 3 subdomains. Refinement at the corner. Error $|e_1^{12}(x)|$ with **COC** after 12 iterations, with $|e^{12}|_\infty = 7.88 \times 10^{-7}$.